Biofabrication

International Society for Biofabrication

PURPOSE-LED PUBLISHING™

Melt electrowriting scaffolds for investigating Schwann cell-mediated modulation of vascular network formation

To cite this article: Hao Wu *et al* 2026 *Biofabrication* **18** 025010

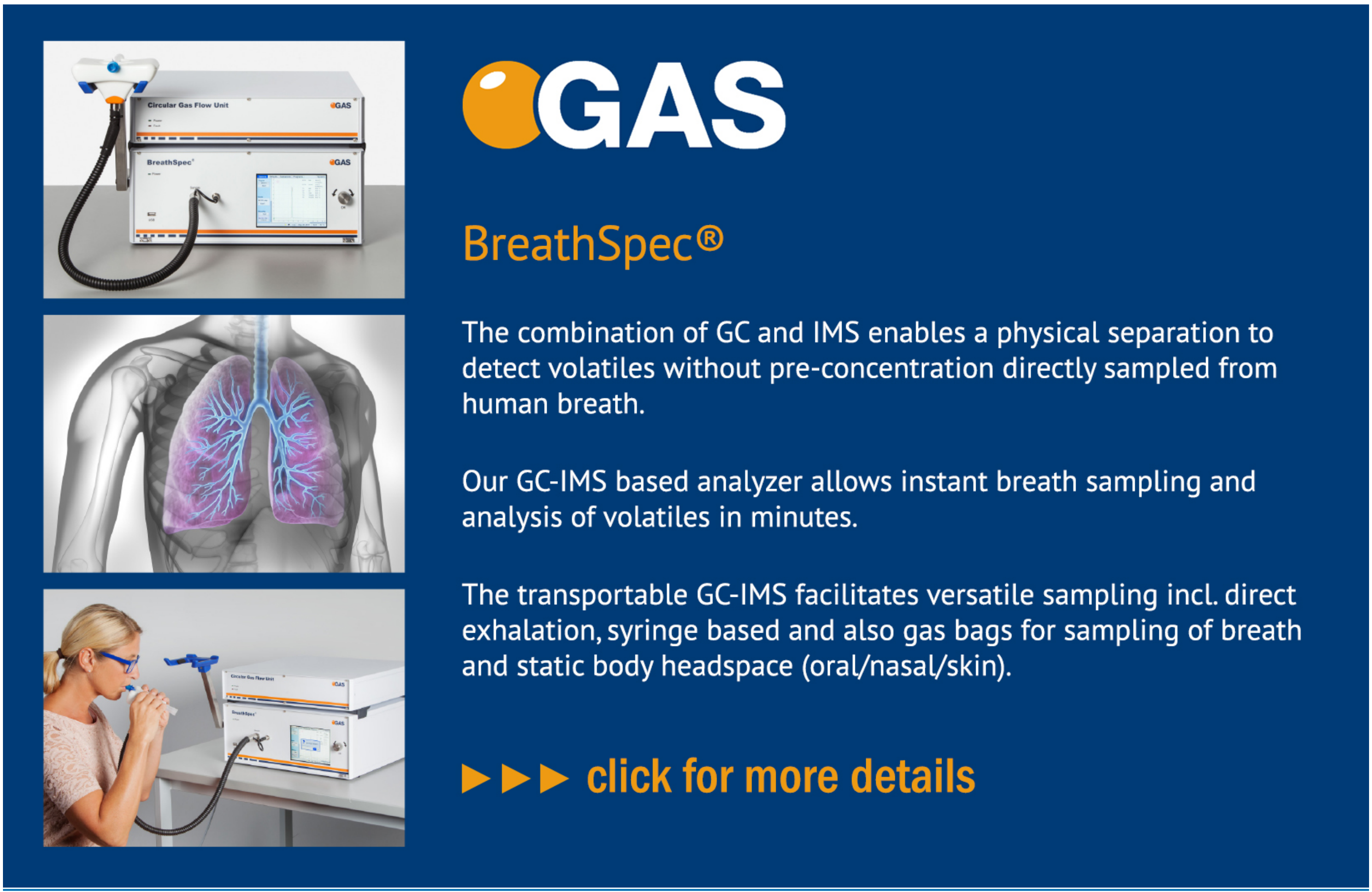

IOP Publishing *Biofabrication* **18** (2026) 025010 https://doi.org/10.1088/1758-5090/ae4ccc

Biofabrication

OPEN ACCESS

RECEIVED
20 November 2025

REVISED
31 January 2026

ACCEPTED FOR PUBLICATION
3 March 2026

PUBLISHED
16 March 2026

PAPER

Melt electrowriting scaffolds for investigating Schwann cell-mediated modulation of vascular network formation

Hao Wu[1], Nathalie Dirkx[2], Esther Wolfs[2], Lorenzo Moroni[1] and Paul Wieringa[1,*]

[1] Complex Tissue Regeneration Department, MERLN Institute for Technology Inspired Regenerative Medicine, Maastricht University, Maastricht 6229ER, The Netherlands
[2] Laboratory for Functional Imaging & Research on Stem Cells (FIERCE Lab), Biomedical Research Institute (BIOMED), Hasselt University, 3590 Diepenbeek, Belgium
[*] Author to whom any correspondence should be addressed.

E-mail: p.wieringa@maastrichtuniversity.nl

Keywords: melt electrowriting, Schwann cells, vascular network formation, endothelial cells

Supplementary material for this article is available online

Abstract

Vascularization remains a major challenge in tissue engineering, restricting both the functional integration of grafts as well as the physiological relevance of *in vitro* models. Inspired by the crucial role of Schwann cells (SCs) in guiding vascular development, we investigated their influence on the vascular network formation of human microvascular endothelial cells (HMVECs). Using melt electrowriting (MEW), we fabricated scaffolds consisting of a single layer of parallel fibers to mimic the oriented axons of the peripheral nerve. A suspended seeding approach was carried out to ensure rat-derived SCs adhered specifically to the fibers, creating parallel arrays with SCs exhibiting strong attachment, viability, and upregulation of myelination-, neurotrophic-, and pro-angiogenic-related genes. A customized system was built to co-culture SCs-laden scaffolds with HMVECs seeded on a hydrogel (2D) and *in* a hydrogel (3D). The parallel fiber distances were varied to assess the spacing of the SC arrays that impacted HMVEC organization. The results revealed that SCs on MEW scaffolds exhibited enhanced expression of key genes compared to a 2D monolayer control. Further, these SC-laden scaffolds significantly enhanced HMVEC network formation in both 2D and 3D environments, with reduced fiber distance showing stronger pro-angiogenic responses. To evaluate species differences, human dental pulp stem cell-derived SCs (HDPSC-SCs) were compared with rat primary SCs. HDPSC-SCs not only showed enhanced expression of pro-angiogenic genes on the scaffold but also promoted superior network formation compared to rat SCs. Collectively, our findings highlight the ability of MEW scaffolds to both pattern SC growth and stimulate a pro-regenerative SC phenotype as a strategy to modulate vascular network formation. This provides a foundation for using the patterning of SCs to drive neurovascular organization for *in vitro* models and more broadly as an approach of regenerative medicine.

1. Introduction

Lack of vascularization remains one of the most critical challenges in tissue engineering [1, 2]. Clinically, engineered grafts often fail after implantation due to poor integration with host tissues and insufficient oxygen and nutrient supply, which ultimately causes inner graft necrosis [3]. For example, in nerve repair, pre-vascularized nerve grafts supplemented with endothelial cells (ECs) or angiogenic growth factors have shown improved nerve regeneration across large defects [4–6]. Similarly, sufficient vascularization in skin tissue engineering avoids graft infections and promotes wound healing [7, 8]. From an *in vitro* model perspective, the absence of vasculature also limits the physiological relevance of disease models. Human tissues like skin and bone are highly vascularized *in vivo*, but their *in vitro* equivalents often lack vascular networks, leading to a limited culture period and impaired capacity to replicate disease processes. For instance, skin models without vasculature cannot replicate the chronic wound healing process

[9, 10], while bone models fail to recapitulate the vascular support required for osteogenesis [11, 12]. ECs play a central role in forming vascular networks for oxygen and nutrient delivery [13, 14]. However, current approaches that incorporate ECs into scaffolds or hydrogels often result in immature and unstable vessels [15, 16]. The main challenges lie in achieving long-term stability with appropriate supporting cells and controlling vascular network patterning to ensure physiological relevance, both *in vitro* and after transplantation [4, 17].

In vivo, nerves and blood vessels are closely associated, forming highly interactive networks [18, 19]. In the peripheral nervous system (PNS), where nerves are richly vascularized, successful nerve regeneration relies on coordinated revascularization to restore metabolic support. This structural and functional coupling is mediated by a wide range of signaling molecules and receptors, ensuring coordinated tissue growth, repair, and regeneration [19, 20]. Vascular development begins with vasculogenesis, where the initial capillary plexus is formed by *in situ* differentiation of hemangiogenic stem cells. This is followed by angiogenesis, during which ECs proliferate, migrate, and remodel into more mature vascular structures [21, 22]. During this process, sensory nerves have been shown to invade the capillary plexus, resulting in the release of paracrine cues that recruit ECs to align with the nerves and subsequently differentiate into stable vascular structures [23, 24]. Investigations into these mechanisms have revealed that Schwann cells (SCs), the principal glial cells of the PNS, are also the key mediators of the paracrine signaling driving this process [23].

Beyond the essential role in nerve myelination and regeneration, SCs also act as a potent regulator in modulating vascular network formation. They secrete various pro-angiogenic factors, such as CXCL12 [25], VEGF-A [26], and ANGPT1 [27], that promote EC survival, migration, and vessel maturation [23, 28]. This dual role makes SCs a unique cell type in mediating neurovascular interactions. However, the isolated contribution of SCs in regulating vascular network formation is difficult to assess, as they are usually studied within the context of nerve tissue. *In vitro* neurovascular models have provided valuable insights, but most rely on rat SCs (RSCs), which limits the translational relevance [29, 30]. Moreover, isolating and expanding primary human SCs remains technically challenging and requires invasive tissue harvesting procedures, which raises ethical concerns and restricts their broader application in tissue-engineered models [31, 32]. To address this limitation, human dental pulp stem cells (HDPSCs) isolated from third molar extraction have been successfully differentiated into functional myelinating SC-like cells (HDPSC-SCs) [33]. These HDPSC-SCs have been shown to myelinate neurites and support neural outgrowth *in vitro*, making them a valuable and accessible human cell source for studying neurovascular interactions [34].

SCs in peripheral nerves exhibit a highly organized longitudinal alignment along axons, forming structural and functional units that regulate nerve conduction and regeneration [35, 36]. The spatial density of aligned SC structures varies depending on anatomical contexts, from densely packed nerve bundles to more dispersed configurations in fascicles and branching neurites. Following nerve injury, SCs rearrange into longitudinal cellular cords known as the Bands of Büngner, which serve as guidance tracks for regenerated axons [35]. Recapitulating such aligned and spatially regulated microstructures *in vitro* is therefore essential for understanding SC behavior and their interactions with other cells. Synthetic scaffolds have therefore been widely used to guide SC alignment and study their interactions with neural and vascular microenvironment [37, 38]. In terms of creating bespoke and oriented polymer scaffolds, melt electrowriting (MEW) has emerged as a promising strategy in tissue engineering and, in particular, in nerve research [39, 40]. MEW enables the fabrication of microscale fiber scaffolds with precise control over fiber diameter, defined distance, and orientation [41]. By depositing fibers in designed patterns, MEW scaffolds can mimic the oriented structures of peripheral nerves and provide structural cues to activate SCs [42, 43]. In contrast to the classical electrospinning technique, MEW enables the fabrication of scaffolds with diameters between 2–50 μm in a solvent-free manner by adjusting parameters such as voltage, pressure, and velocity [41, 44].

Recent studies have applied MEW scaffolds in nerve regeneration research, for example, MEW scaffolds with suspended fibers were generated to support mouse dorsal root ganglion (DRG) explants and SCs, to observe the migration process of SCs and neuronal outgrowth [45]. However, despite the growing use of MEW in tissue engineering, many existing studies employ multilayer grid or woodpile scaffold architectures in which multiple geometric parameters (e.g., fiber diameter, pore size, and overall architecture) are varied simultaneously, making it difficult to isolate the biological effects of individual topographical cues [46]. For instance, previous research has fabricated scaffolds containing multiple regions with different fiber diameters and pore sizes, demonstrating that smaller pores stimulated more cell proliferation than larger pores [47]. Similarly, another study reported pore-size-dependent cell attachment, but the observed effects were also influenced by fiber sagging, highlighting the challenge of disentangling structural variables in conventional MEW scaffold designs [48]. While valuable, such approaches do not closely mimic the structural organization of many native tissues, and the simultaneous variation of multiple parameters limits mechanistic understanding of how individual topographical cues affect cell behavior [46].

In this study, we employed MEW to construct a region-specific scaffold architecture inspired by the aligned organization of SCs in PNS. Rather than using microfibers as surrogate neurons, we utilized them as precisely controllable topographical tools to model variations in SC alignment spacing. The scaffold consists of a single layer of parallel fiber functional region for SC guidance and a mechanically reinforced supporting region. By maintaining a constant fiber diameter and systematically varying only fiber distance, we isolated fiber distance as an independent topographical parameter and decoupled guidance cues from structural support. Using this scaffold, we investigated how SCs modulate vascular network formation of human microvascular ECs (HMVECs) in both 2D and 3D environments. Furthermore, we compared RSCs with HDPSC-SCs to better understand species-specific differences in angiogenic regulation. Together, this work establishes a physiology-inspired MEW neurovascular platform and shows how design-driven scaffold architecture can transform MEW from a fabrication method to a biologically instructive platform for studying neurovascular interactions.

2. Materials and methods

2.1. Fabrication of MEW scaffolds

Scaffolds used in this study were designed using a customized Python code. Each scaffold was printed with 3 layers: (1) monolayer parallel fibers; (2) grid fibers; (3) surrounding rings (figure 1). Depending on the fiber distance between parallel fibers, the scaffolds were set into 4 groups: 300 μm, 500 μm, 700 μm, and 900 μm. The parallel fibers area is the functional region used for SCs seeding, which contains a single fiber that crosses and attaches all parallel fibers to keep the fiber distance constant. The grid fibers and surrounding rings are the supporting region to hold the scaffold, retaining its original shape and easily handled with tweezers.

Poly(ε-caprolactone) (PCL) (average Mn 80 000 g mol^{-1}, Sigma-Aldrich) pellets were used with the MEW printer (Spraybase® A-1204-0000) to make scaffolds. 1.4 g of PCL was loaded into the heating metal syringe fitted with a bronze nozzle (0.15 mm, E3D online) and set to 180 °C for 3 h. Before starting printing, the metal collector was covered with an aluminum foil sheet to collect scaffolds. The distance between the nozzle and the collector was kept at 5.5 mm, and the pressure was set to 1.0 bar. MEW parameters for fabricating different layers of scaffolds are mentioned in table S1. The experiments were processed at 25 °C, and the humidity was set around 35%.

The increased processing temperature and heating time were employed due to the higher molecular weight of the PCL used in this study, which differs from the lower-molecular-weight PCL commonly reported in MEW literature [49–51]. Lower temperatures were insufficient to ensure steady fiber extrusion and homogenous melting, according to preliminary optimization. Instead, heating at 180 °C for 3 h consistently yielded a uniform melt suitable for repeatable printing. To minimize thermal degradation, scaffold fabrication was restricted to within 2.5 h following complete melting.

2.2. Characterization of MEW scaffolds

The parallel fibers area of scaffolds was detected by scanning electron microscope (SEM) (JSM-IT200 InTouchScope$^{\text{TM}}$, JEOL). Before scanning, the scaffolds were prepared with the gold sputterer (108 Auto, Ted Pella) at 30 mA for 80 s. The fiber distance and the diameter were analyzed using Fiji software.

2.3. Fabrication of SCs seeding and co-culture molds

To seed SCs on the parallel fibers, customized polydimethylsiloxane (PDMS) seeding molds were made (figure S1(a)). The seeding molds are composed of a top and bottom unit. Briefly, the negative mold was created by milling a poly (methyl methacrylate) slab with the milling machine (SRM-20, Roland). PDMS solution was prepared freshly by mixing monomer and curing agent in a 10:1 (w/w) ratio. After vacuuming to remove the air bubbles, the PDMS solution was poured into the negative mold and cured at 80 °C for 2 h. Afterwards, the seeding molds were peeled off and post-cured/sterilized at 160 °C for 2 h.

To co-culture SCs and HMVECs, the co-culture molds were fabricated as above (figure S1(b)). After being cured at 80 °C, the PDMS co-culture molds and 32 mm diameter round coverslips were washed with distilled water, 70% ethanol, and acetone to remove accumulated dust on the surface. Next, a jet of nitrogen was applied to quickly blow off the acetone left on the PDMS or glass surface. PDMS co-culture molds and coverslips were placed inside the plasma cleaner (Femto PCCE, Diener), with the parts that will be in contact facing up. Being treated with the air supply at 0.5 mbar and 60 W for 1 min, the coverslips and PDMS co-culture molds were bonded together with tweezers. Then co-culture molds were post-cured/sterilized at 160 °C for 2 h.

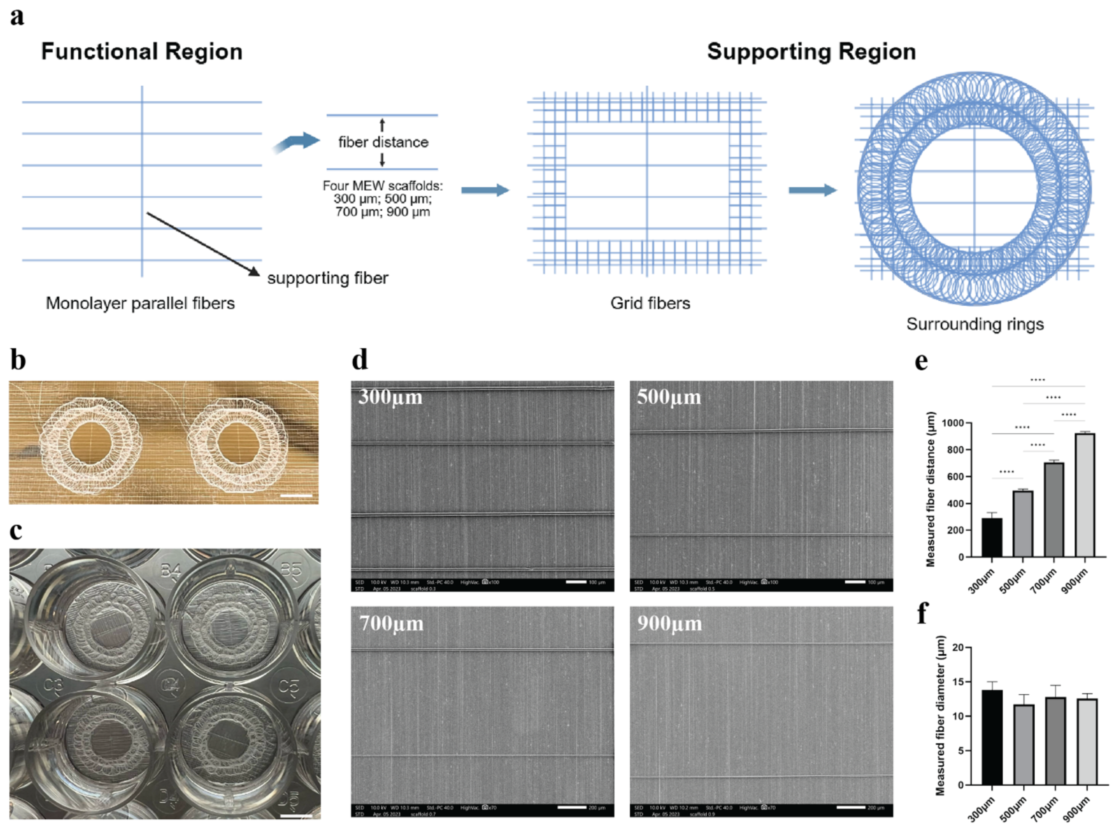

Figure 1. Fabrication process and morphology of the MEW scaffolds. (a) Scheme of the MEW scaffolds fabrication process. According to the fiber distance between parallel fibers, the scaffolds were set to 4 groups: 300 μm, 500 μm, 700 μm, and 900 μm. Created in BioRender. Wu, H. (2026) https://BioRender.com/uwv24w1 (b) MEW scaffolds were collected on the aluminum foil sheet. (c) MEW scaffolds were transferred to a 24 well-plate. (d) SEM images of MEW scaffolds with different fiber distances. (e) The measured fiber distance between parallel fibers in each scaffold group. (f) The diameter of parallel fibers in each group. Scale bars are 4 mm (b), (c), 100 μm (*d*: 300 μm, 500 μm scaffolds), and 200 μm (*d*: 700 μm, 900 μm scaffolds). $^{****}p < 0.0001$, one-way ANOVA with Tukey's multiple comparisons post-hoc test, $n \geqslant 6$.

2.4. Cell culture

Primary RSCs were isolated from the sciatic nerves of the neonatal Wistar rat pups, following local and Dutch animal use guidelines, and were based on previously described protocols [52–54]. The license registration number 10 700 was used in communication with the Dutch authorities. RSCs were cultured within the RSC medium (RSCM), which was composed of Dulbecco's Modified Eagle Medium (high glucose with GlutaMAX, Gibco) supplemented with 10% (v/v) foetal bovine serum (FBS, Westburg Life Sciences), 1% (v/v) N2 supplement (STEMCELL Technologies), 20 μg ml^{-1} bovine pituitary extract (Gibco), 5 μM forskolin (STEMCELL Technologies), and 100 U ml^{-1} penicillin and 100 μg ml^{-1} streptomycin (Gibco).

HDPSC-SCs were provided by Hasselt University Biomedical Research Institute, and cultured following previously published protocols [33, 34]. Ethical approval was obtained by the medical ethical committee of Ziekenhuis Oost-Limburg, Genk, Belgium (13/0104 U). Following informed consent, third molars were collected from donors undergoing tooth extraction for orthodontic reasons. Briefly, HDPSC-SCs were cultured on a poly-l-lysine-coated flask surface (Sigma-Aldrich). The HDPSC-SCs medium was composed of minimal essential medium (αMEM, Westburg Life Sciences), supplemented with 2 mM L-glutamine, 10% (v/v) heat-inactivated FBS, 10 ng ml^{-1} of basic fibroblast growth factor (immunotools), 5 ng ml^{-1} of platelet-derived growth factor AA (immunotools), 200 ng ml^{-1} of Neuregulin-1 (immunotools), 5 μM forskolin, and 100 U ml^{-1} penicillin and 100 μg ml^{-1} streptomycin.

HMVECs were purchased from Lonza and grown in EC growth medium (EGM, PromoCell). In this study, RSCs, HDPSC-SCs, and HMVECs were cultured at 37 °C and 5% CO_2 environment, and used between passages 4 and 8.

2.5. Scaffolds preparation and SCs seeding

A 15 mm diameter punch was used to cut down the scaffolds. The scaffolds were transferred into a 24 well-plate and sterilized for 2 h in 70% ethanol. Next, the scaffolds were detached from the aluminum foil by tweezers and followed by air drying, PBS washes for 3 times, and then stored in PBS for further use.

For SCs seeding on the scaffolds, we used seeding molds and SC medium supplemented with 10% (w/v) dextran (Pharmacosmos) (figure 2). The bottom unit was placed into the well of 24 well-plate and filled with 22 μl medium in the middle hole. The scaffold was transferred on top of the bottom unit, and the top unit was placed above. A 16 mm outer diameter silicone O-ring (Eriks) was put on top to press the whole pieces tightly. A 48 μl of medium was dropped in the middle hole of the top unit. When SCs reached $\sim$80% confluency, they were trypsinized and resuspended in the dextran medium. For each scaffold, a droplet of 12 μl with 5×10^3 cells was added on top. After 1 d of incubation, the SCs could grow along the parallel fibers of the scaffold. The scaffold was then taken out and washed once with PBS for later use.

2.6. Live/dead staining

To evaluate the cytotoxicity of MEW scaffolds, a live/dead staining kit (Invitrogen) was used after 1 d of seeding SCs. Briefly, PBS was used to dilute Calcein AM and ethidium homodimer-1 (EthD-1) to reach the final concentration of 2 μM and 2 μM, respectively. The staining solution was added to the SC-scaffolds and incubated at 37 °C for 30 min. Then, the samples were washed with PBS and imaged using a fluorescence microscope (Nikon Eclipse Ti-E).

2.7. Cell viability and proliferation assay

To determine the medium used for co-culturing both RSCs and HMVECs, the PrestoBlue assay (Invitrogen) was used to check cell viability after culturing RSCs for 1, 3, and 5 d. RSCs were seeded in the 96 well-plate with a density of 2×10^3 cells per well. RSCs were treated with different ratios of RSCM and EGM (100:0, 75:25, 50:50, 25:75, 0:100). At each time point, the medium was removed from the well and washed with PBS twice. The cells were then treated with PBS and PrestoBlue solution in a 9:1 (v/v) ratio for 30 min in the incubator. Next, 100 μl of the medium was transferred into a black 96 well-plate with a clear bottom. The fluorescence of each well was detected by the plate reader (CLARIOstar, BMG Labtech) at excitation and emission wavelengths of 560 and 590 nm, respectively.

A cell proliferation assay was performed after 1, 3, and 5 d of culturing RSCs with different medium compositions by using CyQUANT Cell Proliferation Kit (Invitrogen). After performing the PrestoBlue assay, samples were frozen at −80 °C and thawed at room temperature (RT) three times. 150 μl of Proteinase K in Tris/EDTA solution was added to each well at 56 °C overnight. The next day, 150 μl of lysis buffer was added to each treated well at RT for 1 h of incubation. Next, 100 μl of the medium was added to a black 96 well-plate with addition of the same volume of 2× GR dye. The sample was protected from light at RT for 15 min. A plate reader was used to detect the fluorescence of the sample at excitation and emission wavelengths of 480 and 520 nm, respectively.

2.8. Effect of MEW scaffolds on SCs viability

To evaluate whether culture on MEW scaffolds affects RSC viability compared with conventional 2D culture, RSCs were seeded onto MEW scaffolds with fiber distances of 300 μm, 500 μm, 700 μm, and 900 μm and cultured for 1 d to allow cell attachment along the parallel fibers. RSCs cultured on standard 96 well-plate served as the 2D control to assess potential effects of scaffold material and fiber distance on cell viability.

Cell viability was assessed using the PrestoBlue assay and normalized to DNA content quantified by the CyQUANT Cell Proliferation Kit, as described in section 2.7. This normalization accounted for differences in cell number between scaffold-based and 2D cultures and enabled quantitative comparison of RSC viability across different scaffolds.

2.9. Quantification of cell coverage on MEW scaffolds

RSCs were seeded on the scaffolds with different fiber distances of 300 μm, 500 μm, 700 μm, and 900 μm for 1 d. Calcein AM was diluted in PBS and added to the SC-scaffolds at 37 °C for 30 min to visualize live cells. Samples were then washed with PBS and imaged by a fluorescence microscope. To evaluate the relative cell coverage in each group, Fiji software was used to analyze the fluorescence intensity (a.u.) along the detected length of the parallel fiber.

2.10. Immunofluorescence staining

Samples were fixed with 4% paraformaldehyde solution at RT for 25 min, rinsed with PBS twice, and stored in PBS for further use. Samples were permeabilized with 1% Triton X-100 in PBS for 5 min, followed by washing with PBS. Next, samples were blocked with a blocking buffer composed of 5% donkey serum, 0.05% Tween-20, and 3% bovine serum albumin (BSA) in PBS at 4 °C overnight under mild agitation. Afterwards, samples were incubated with the primary antibody (human CD31 antibody, 1:200) in the blocking buffer at 4 °C overnight under mild agitation. The next day, samples were washed with washing buffer composed of 0.05% Tween-20 and 3% BSA in PBS, then incubated with secondary antibody (donkey anti-sheep, Alexa Fluor 488, 1:500) in washing buffer at 4 °C overnight under mild agitation. After incubation, samples were washed with PBS 3 times. Phallodin (Alexa Fluor 647, 1:500) was used at RT for 1 h to stain the cytoskeleton. Cell nuclei were labeled with DAPI (0.2 μg ml^{-1}) at RT for 20 min, and samples were left in PBS until imaging. Samples were imaged with a fluorescence microscope or confocal microscope (Nikon Eclipse Ti2 2-photon).

2.11. RNA extraction, reverse transcription, and quantitative RT-PCR

SCs cultured on the scaffolds and 6 well-plate were collected after 1 d for gene expression analysis.

mRNA of SCs was extracted using Trizol reagent (Invitrogen), following the instructions. For scaffold-based cultures, multiple scaffolds were pooled to obtain sufficient RNA yield, with the number of scaffolds adjusted according to fiber distance: six 300 μm scaffolds, eight 500 μm scaffolds, ten 700 μm scaffolds, and twelve 900 μm scaffolds per sample. Briefly, 1 ml of Trizol solution was added to the sample to lyse cells, and stored at −80 °C for further use. Samples were thawed at RT for 5 min and mixed with 200 μl of chloroform. Shaking vigorously for 15 s and being centrifuged at 4 °C for 15 min. The supernatant was transferred to a new tube and mixed with 500 μl of isopropanol to precipitate RNA. The RNA pellet was then washed once with 75% ethanol and air-dried at RT for 30 min. Afterwards, the RNA pellet was resuspended in nuclease-free water, and the RNA concentration was measured using a Nanodrop system (Thermo Fisher Scientific). The RNA was then reverse-transcribed into cDNA with iScript cDNA Synthesis Kits (Bio-Rad) according to the manufacturer's protocol. Quantitative RT-PCR was performed using iQ SYBR Green Supermix on the PCR machine (Bio-Rad). SCs cultured on the well plate were used as a control. Relative mRNA expression levels were analyzed by the $\Delta\Delta$CT method and normalized to β-actin gene expression. The primers of the targeted gene are mentioned in table S2.

2.12. 2D tube formation test

The 2D tube formation test was performed following the instructions from Thermo Fisher Scientific. Briefly, geltrex (LDEV-Free Reduced Growth Factor Basement Membrane Matrix, Gibco) was used to coat the 48 well-plate (150 μl per well) and was incubated at 37 °C for 30 min. Next, HMVECs were seeded on the surface at a density of 4×10^4 cells cm^{-2} in EGM. 16 h after cell seeding, the tube formation structure was imaged with brightfield using a fluorescence microscope.

When culturing HMVECs with MEW scaffolds (SCs-free or SCs-laden), 5 μl geltrex was added to the middle well of the co-culture mold. The scaffolds were then transferred immediately to the co-culture mold with parallel fibers placed on top of the geltrex surface. A 14.5 mm outer diameter silicone O-ring (Eriks) was put on top to ensure the scaffold's position. After incubating at 37 °C for 30 min, HMVECs were seeded on top with 5×10^3 cells in 20 μl EGM. Next, the samples were imaged with brightfield after 16 h.

2.13. 3D tube formation test

The 3D tube formation test was performed using the co-culture mold based on the 2D tube formation protocol mentioned above. Briefly, after transferring MEW scaffolds (SCs-free or SCs-laden) on 5 μl geltrex with an O-ring on top, the samples were incubated in the incubator for 30 min. Next, 20 μl of neutralized collagen solution composed of collagen I (1.5 mg ml^{-1}, Corning), 1 × PBS, and EGM containing 2×10^6 cells ml^{-1} of HMVECs was loaded on top and incubated at 37 °C for 30 min to crosslink. The samples were filled with 200 μl EGM to culture for 3 d. To visualize the morphology of HMVECs inside the collagen hydrogel, immunofluorescence staining was performed with CD31 (marker of ECs), phalloidin (cytoskeleton), and DAPI (cell nuclei). Samples were imaged with a confocal microscope.

2.14. Image analysis

For 2D tube formation images, brightfield images were taken, focusing on the vascular networks formed between the parallel fibers as regions of interest (ROIs), excluding the supporting fiber and the supporting region. Each scaffold selected at least four ROIs for imaging. Within each image, the regions between two parallel fibers were cropped for subsequent analysis. Fiji (angiogenesis analyzer plugin) was used to objectively assess endothelial networks by extracting network characteristics (figure S2). The plugin detects extremities (extremities in a binary skeleton), junctions (groups of joined nodes, pixels with at least three neighbors), branches (elements delimited by a junction and one extremity), and segments (elements delimited by two junctions) [55]. Next, we analyzed the number of junctions, total length, and total segment length in each cropped image. These values were normalized to the area of the corresponding cropped region. For each scaffold, the averaged values from all cropped images were used to represent its 2D tube formation results.

For 3D tube formation images, fluorescence images with z-stacks (z-step: 5 μm, z-range: 50 μm) were captured. For each scaffold, at least four ROIs were imaged. The CD31 channel was extracted and converted into a 2D max intensity projection. Fiji (AngioTool 2.0 plugin) was used to analyze three key parameters: vessel area percentage, number of junctions, and total length (figure S2) [56]. These values were normalized to the region area for each image, and the results from all ROIs per scaffold were averaged to represent its overall 3D tube formation results.

2.15. Statistical analysis

The data presented in this study were shown as mean ± SD and were analyzed using GraphPad Prism 10 software. Each experiment was repeated at least three times using biologically independent samples. Statistical analysis was performed using unpaired t-test, one-way ANOVA with Tukey's multiple comparisons post-hoc test, and two-way ANOVA with multiple comparison analysis using Tukey's post-hoc test ($^{*}p < 0.05$, $^{**}p < 0.01$, $^{***}p < 0.001$, $^{****}p < 0.0001$).

3. Results

3.1. Fabrication and morphology of MEW scaffolds

The fabrication of the MEW scaffolds contained three steps (figure 1(a)). First, a single layer of parallel fibers was deposited to form the central functional region, which served as the interface for SCs seeding and co-culture experiments. This region was designed to model variations in the spatial spacing of aligned SC structures. Four scaffold groups with defined fiber distances (300 μm, 500 μm, 700 μm, and 900 μm) were fabricated to represent different levels of SC alignment density. To retain stable fiber distances throughout the whole experiment process, a single supporting fiber was printed across the parallel fibers. Subsequently, grid fibers and surrounding rings were added to form a structural supporting region, improving mechanical stability and handling while leaving the central area unobstructed for biological interactions (figures 1(b) and (c)). This region-specific architecture differs from traditional electrospun or multilayer MEW scaffolds, which are typically made up of multilayered fiber meshes and handled as homogeneous bulk constructs [47, 48, 57, 58]. By spatially separating topographical guidance (functional region) from mechanical reinforcement (supporting region), our design enables precise control of SC–fiber interactions while maintaining scaffold integrity.

SEM images confirmed the successful fabrication of all scaffold groups, showing well-organized parallel fibers (figure 1(d)). As shown in figure (e), the measured fiber distances were 290.71 ± 42.02 μm, 497.38 ± 10.59 μm, 707.33 ± 14.57 μm, and 924.44 ± 11.16 μm, closely matching the preset values. The diameters of the parallel fibers did not differ significantly across groups, with the averages of 13.81 ± 1.18 μm, 11.70 ± 1.45 μm, 12.78 ± 1.72 μm, and 12.75 ± 0.72 μm, respectively (figure 1(f)). These results demonstrate the high accuracy of MEW in printing fibers at defined positions.

However, we also observed technical limitations when printing scaffolds. When setting fiber distances below 300 μm, fiber bridging frequently occurred, caused by residual charges in freshly deposited fibers interfering with subsequent fiber placement [59]. This phenomenon limited the minimal practical fiber distances, and therefore, 300 μm was finally selected as the smallest fiber distance used in this study.

To improve handling and ensure structural stability, the parallel fibers were reinforced with supporting fibers, grid fibers, and supporting rings. The supporting fibers were critical, as scaffolds without them often showed tangling parallel fibers after detachment from the aluminum foil, making them unsuitable for further use. Grid fibers helped stabilize the surrounding region of the parallel fibers and restricted their excessive flexibility. However, using grid fibers alone to reinforce scaffolds was insufficient, as scaffolds often tended to fold themselves when manipulated with tweezers, particularly in aqueous conditions. This challenge was effectively solved by the addition of outer supporting rings, which substantially improved scaffold integrity and ease of handling.

The fabricated fiber diameters (~12 μm) were close among the four groups (no significant differences) and fell within the physiological range of peripheral nerve fibers, which vary between 2–20 μm for myelinated axons and 0.2–1.2 μm for unmyelinated nerve fibers [60, 61]. Thus, the MEW scaffolds not only provided reproducible and mechanically stable structures but also presented as axon-like topographical cues, indicating their suitability for subsequent SCs seeding and neurovascular modeling.

Fiber diameter is recognized as an important geometric characteristic that can independently affect SC behavior [62–64]. In peripheral nerves, axon diameter critically influences SC ensheathment and myelination, highlighting its importance in SC maturation and function [64–66]. Previous research used electrospun fibers with diameters ranging from 300 nm to 1300 nm showed that increasing fiber diameter influences SC morphology, cytoskeletal organization, focal adhesion formation, filopodia development, migration, and proliferation. For instance, SCs cultured on larger diameter fibers exhibited more elongated morphology, enhanced filopodia formation, and increased motility, while their proliferation rate was reduced compared with cells on smaller diameter fibers [63]. Compared with electrospinning, MEW typically produces fibers in the micrometer range (approximately 2–50 μm), with diameter controlled by parameters such as melt temperature, nozzle size, voltage, and collector distance, pressure, and extrusion rate. In particular, melt temperature, which governs polymer viscosity, together with extrusion rate, plays a critical role in determining filament stability and is reported to have the greatest impact on fiber diameter [41]. MEW studies have further demonstrated that micrometer-scale suspended fibers (~50 μm in diameter) can guide DRG explant-derived SC migration and interaction with neuronal structures, emphasizing the biological relevance of diameter-controlled topographies [45]. In the present study, fiber diameter was intentionally maintained at comparable values across all scaffold groups to ensure that observed differences in SC behavior and angiogenic responses were primarily attributed to variations in fiber distance rather than confounding geometric factors.

3.2. SC response to MEW scaffolds

To enable efficient SCs seeding on the MEW scaffolds, we designed a custom PDMS seeding mold

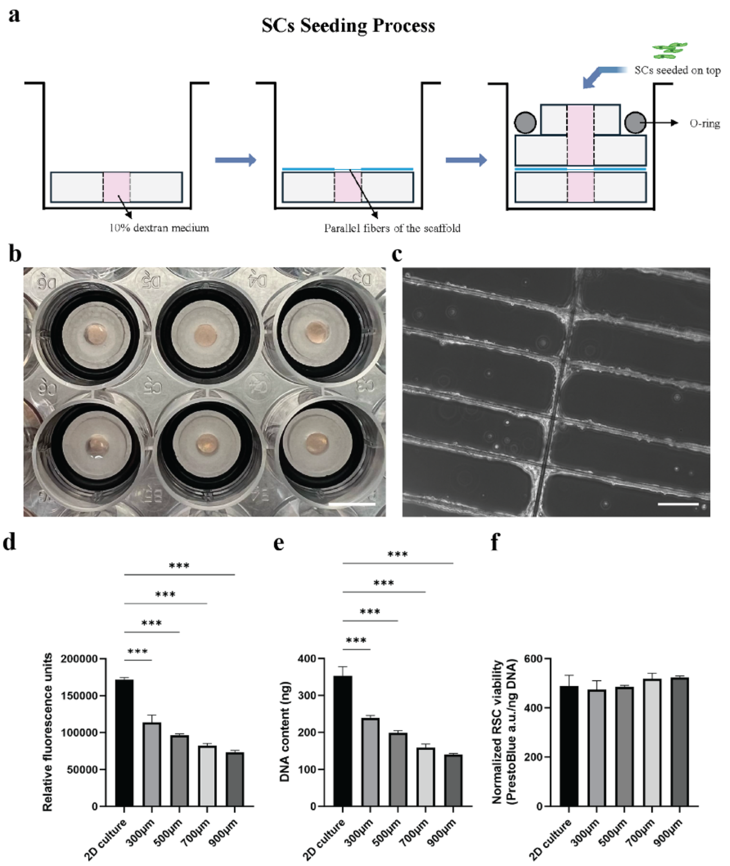

Figure 2. SCs seeded on the MEW scaffolds. (a) Scheme of the SCs seeding process with the seeding molds. (b) The seeding system was assembled in a 24-well plate. (c) After being seeded for one day, the RSCs-laden scaffolds were washed with PBS. Viability (d), proliferation assay (e), and normalized RSC viability (f) of RSCs on MEW scaffolds compared to 2D culture. $***p < 0.001$, one-way ANOVA, $n = 3$. Scale bars are 8 mm (b), and 300 μm (c).

(figure S1(a)). The initial attempts were to directly place scaffolds at the bottom of well plates, which led to the formation of a cell monolayer between the parallel fibers. During subsequent handling and transferring, this monolayer was inevitably carried along with the scaffold, which opposed our aim of obtaining SCs attachment only on the parallel fibers. By contrast, suspending the scaffolds in the PDMS mold (between top and bottom units) induced cell attachment directly onto the fibers (figure 2(a)). To further improve cell attachment and uniform distribution, the SC medium was supplemented with 10% dextran, which increases viscosity and reduces cell sedimentation. This strategy, previously reported to enhance seeding efficiency on 3D polymer scaffolds, solved common challenges such as poor initial cell attachment, cell sedimentation, and uneven cell distribution caused by scaffold porosity [67, 68]. Here, the usage of dextran in seeding media successfully facilitated homogenous SCs seeding, with RSCs gradually settling and wrapping around the suspended fibers (figures 2(b) and (c)).

As shown in figures 2(d) and (e), cell viability and proliferation assays revealed that RSCs cultured under standard 2D conditions exhibited the highest overall cell viability and proliferation compared with RSCs cultured on MEW scaffolds. Among the four MEW scaffold groups, the 300 μm fiber distance showed the highest viability and proliferation, followed by the 700 μm and 500 μm groups, whereas the 900 μm group exhibited the lowest values. Importantly, normalized RSC viability demonstrated no statistically significant differences between cells cultured on MEW scaffolds with different fiber distances and those cultured under 2D conditions (figure 2(f)), indicating that the PCL scaffold material and the variation in fiber distance did not compromise RSC viability. The observed differences in cell viability and proliferation among the MEW groups are likely attributable to variations in the effective functional area and fiber density within the scaffold. Specifically, the 300 μm group contained a higher number of parallel fibers within the functional region compared with the other groups, which may have provided increased adhesion sites supporting RSCs to grow.

Live/dead staining was performed after seeding RSCs for one day. As shown in figure 3(a), RSCs already adhered to the parallel fibers, with the great majority of cells remaining viable. To evaluate

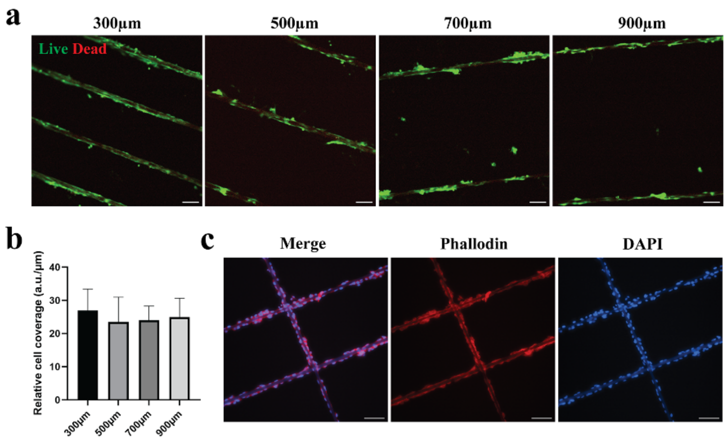

Figure 3. The behavior of RSCs on the MEW scaffolds. (a) Live/dead staining of the RSCs on the scaffolds. Live cells were labeled with Calcein AM (green) and dead cells were labeled with EthD-1 (red). (b) The relative cell coverage among the 4 groups of MEW scaffolds. $P > 0.05$, one-way ANOVA, $n = 3$. (c) Immunofluorescence staining of the RSCs on the 300 μm scaffold. RSCs were stained with Phalloidin (red) and DAPI (blue). Scale bars are 100 μm (a)–(c).

whether fiber distances could influence SCs attachment, quantitative analysis of live cell coverage (live cell fluorescence intensity normalized to the detected fiber length) was carried out. This revealed no significant differences between the four scaffold groups (figure 3(b)). While accurate counting of cell nuclei along the fibers to quantify cell coverage was prevented by autofluorescence from the PCL fibers in the DAPI channel. Besides, Phalloidin and DAPI staining qualitatively revealed that RSCs settled along the fibers with uniform cell distribution (figure 3(c)).

To investigate whether the fiber environment influenced SC behavior, gene expression profiles were compared between RSCs cultured on MEW scaffolds with different fiber distances and conventional 2D monolayer cultures. After 1 d of culture, RSCs had adhered and aligned along the fibers across all scaffold groups (figure 4(a)). As shown in figure 4(b), gene expression levels were largely comparable among the different scaffold groups, with only slight differences observed. In particular, c-Jun expression showed a modest increase in RSCs cultured on the 300 μm scaffolds, although the magnitude of change was limited. Compared with monolayer culture, RSCs on the MEW scaffolds showed significant upregulation of multiple genes associated with SC phenotype and angiogenic signaling, including MBP, BDNF, GDNF, CXCL12, VEGF-A, and ANGPT1, while Krox20 showed a tendency of upregulation (no significant difference). Notably, VEGF-A showed a pronounced upregulation, with an approximate 12–15-fold increase in expression. In contrast, NGF expression was significantly reduced in RSCs cultured on the MEW scaffolds.

Among these genes, c-Jun plays a critical role in promoting SCs dedifferentiation and activating a repair program after nerve injury by suppressing myelination, enabling the formation of bands of Büngner, and axon regrowth [69, 70]. Following nerve injury, distal axon segments undergo Wallerian degeneration, during which SCs in the distal stump dedifferentiate, align along the basal lamina, and form bands of Büngner that serve as natural scaffolds guiding axonal reinnervation [36]. Notably, the structure of these bands has been found to be controlled by c-Jun, emphasizing its central role in coordinating the SC repair phenotype [71]. In contrast, Krox20 is a key regulator of myelination, activated by axonal signals to drive the transition of immature SCs into myelinating cells. Studies have shown that Krox-$20^{-/-}$ SCs fail to myelinate properly [70]. Notably, previous studies have shown that c-Jun and Krox20 exert antagonistic functions in SCs, with c-Jun promoting a repair state and Krox20 driving a myelinating phenotype [69, 70, 72]. MBP, a key component of the myelin sheath, serves as a marker of SCs. It has been reported to be detectable in early passages and further enhanced in myelinating states *in vitro* [73]. Consistently, MBP expression was upregulated across all scaffold groups, indicating that the fiber environment generally promoted a shift toward a myelination-related phenotype. Notably, only RSCs cultured on the 300 μm scaffolds showed elevation of c-Jun, suggesting that a narrower fiber distance could trigger a dual response combining both repair and myelination features. This indicates that RSCs were highly responsive to the axon-like topographical cues provided by the fibers.

Neurotrophic factors such as BDNF, NGF, and GDNF can be secreted by SCs and play essential roles in neuronal survival, axonal growth, and nerve regeneration in the PNS, particularly following nerve injury [74]. For example, elevated BDNF levels have been reported to prevent neuronal death and promote axon elongation, whereas reduced BDNF expression suppresses neurite outgrowth and impairs axon regeneration [75]. Similarly, GDNF expression

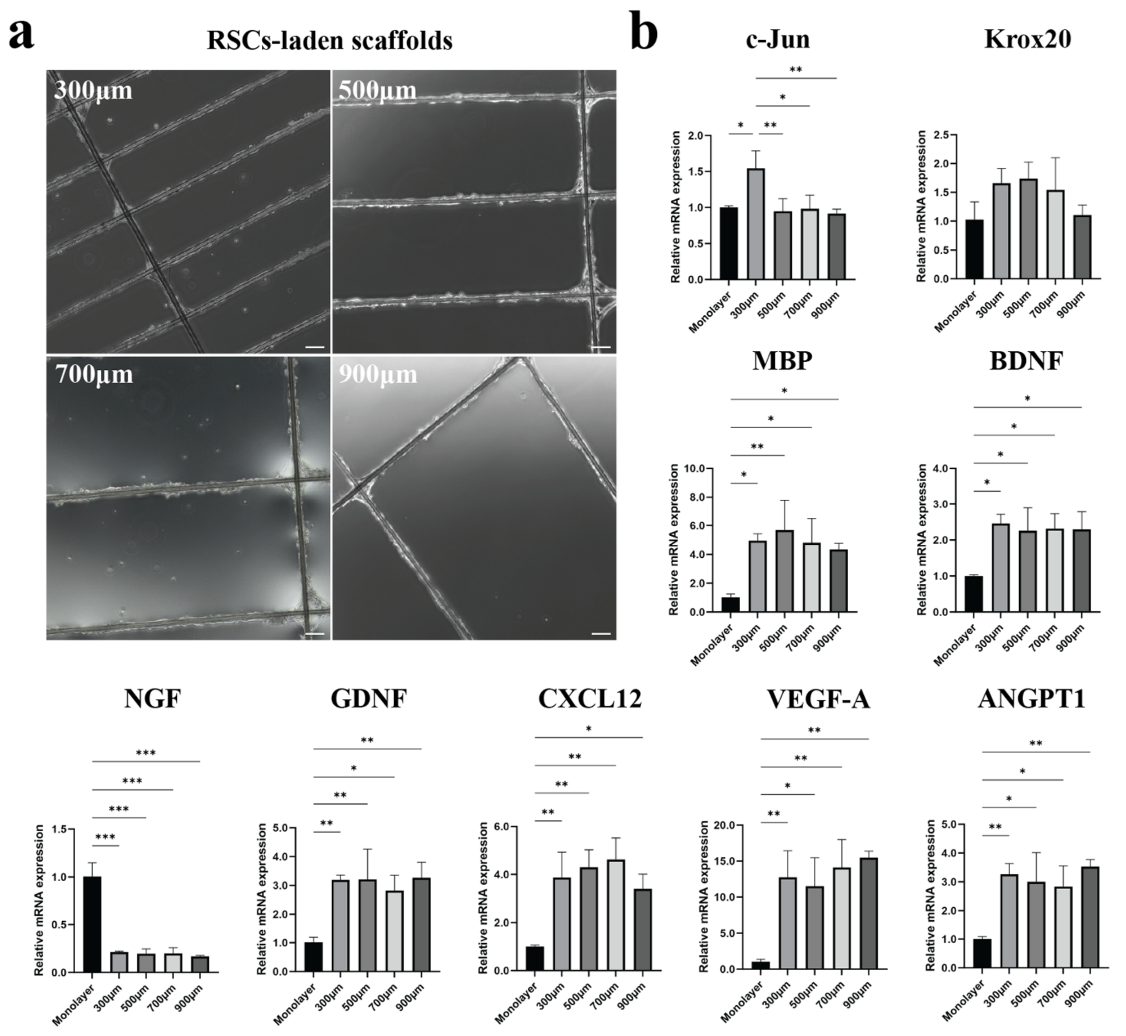

Figure 4. Gene expression profile of RSCs cultured on MEW scaffolds and in 2D monolayer conditions after 1 d. (a) Gross morphology of RSCs-laden MEW scaffolds after 1 d of culture. (b) Relative mRNA expression of nine genes in RSCs cultured on MEW scaffolds compared with conventional 2D monolayer culture after 1 d. Scale bars are 100 μm (a). $^{*}p < 0.05$, $^{**}p < 0.01$, $^{***}p < 0.001$, one-way ANOVA with Tukey's multiple comparisons post-hoc test, $n = 3$.

is markedly increased in SCs after sciatic nerve transection in rats, promoting axonal repair [76]. In our study, both BDNF and GDNF were significantly upregulated in scaffold-seeded RSCs, suggesting that the fiber environment triggered a neuro-supportive mode of RSCs. Interestingly, NGF expression was significantly downregulated under the same conditions. The upregulation of NGF in SCs is typically associated with early nerve development while a decrease in expression has been observed upon nerve maturation [77, 78]. NGF downregulation, together with increased BDNF and GDNF, may reflect a shift from an immature toward a more differentiated SC phenotype. Although the specific mechanism in our system is unknown, our findings suggest that the scaffold microenvironment may regulate the balance of neurotrophic signaling, preferring BDNF- and GDNF-mediated pathways over NGF.

Notably for neurovascular development, the expressions of pro-angiogenic factors CXCL12, VEGF-A, and ANGPT1 were significantly upregulated when RSCs were cultured on fibers. It has been demonstrated during the mice development phase, SCs and sensory nerves could invade the capillary plexus and secrete CXCL12, which recruits ECs to align with nerves. Subsequent secretion of VEGF-A further induces arterial differentiation in the nerve-associated vessels [23, 24]. ANGPT1, typically produced by pericytes, serves as a stabilizing factor that promotes pericyte-EC interactions, vessel maturation, and lumen formation [79]. These findings suggest scaffold-seeded RSCs may contribute to the vascular network formation by enhancing ECs recruitment, sprouting, and stabilization.

Together, these results indicate that MEW scaffolds provide a biomimetic architectural environment that promotes SCs attachment, viability, and activation of both myelination- and neurotrophic-related gene expression. Moreover, the observed upregulation of pro-angiogenic genes suggests that RSCs-laden scaffolds could serve as a pro-angiogenic niche, supporting vascularization in both engineered models and potential *in vivo* applications.

3.3. Influence of RSCs on HMVEC network formation

To determine suitable media for co-culturing both RSCs and HMVECs, PrestoBlue and DNA quantification assays were performed to evaluate cell viability and proliferation under different medium ratios (RSCM: EGM = 100:0, 75:25, 50:50, 25:75, 0:100) over 1, 3, and 5 d (figure S3). At day 1, there were no differences among groups in either cell viability or DNA content. By day 3 and day 5, both assays showed that mixed media significantly enhanced RSC viability and DNA content compared to either RSCM or EGM alone. Interestingly, RSCs cultured in EGM alone showed comparable viability and proliferation to those in RSCM across all time points. Since EGM is also optimized for endothelial culture, it was finally selected as the co-culture medium.

To investigate the effect of RSCs-laden scaffolds on HMVECs network formation, a 2D test was first performed using geltrex, a basement membrane extract rich in laminin, collagen IV, entactin, and heparan sulfate proteoglycans, commonly used to induce endothelial capillary-like network formation [80–82]. Usually, when ECs are seeded on geltrex, they spontaneously form network structures that typically persist around 24 h before degrading [82, 83].

In our study, a customized PDMS co-culture mold was designed for the tube formation test (figure S1(b)). The mold contained a shallow circular well (4 mm diameter, 0.4 mm height) that could be filled with 5 μl of geltrex, producing a flat gel surface. In regular well plates, the meniscus effect causes the liquid surface to curve upward along the edges, leading to uneven gel thickness and pooling of cells in the center [82]. By contrast, our mold eliminated this effect, producing a uniform, flat gel substrate. This improved imaging quality, facilitated reproducibility, and handling. Most critically, this ensured uniform contact between SCs-laden scaffolds and the gel surface.

2D tube formation tests were performed for 16 h, with following parameters being analyzed: number of junctions (indicating sprouting activity), total length (the sum of branches and segments, reflecting overall elongation), and total segment length (connections between two junctions, reflecting elongation of main structures) [55, 80].

Brightfield images indicated different network formation responses depending on scaffold fiber distances and the presence of RSCs (figure 5(a)). When MEW scaffolds were not seeded with RSCs, HMVECs tended to spread as a monolayer, particularly in the 900 μm group, rather than creating branched networks (figures 5(b)–(d)). While scaffolds with 500 μm and 700 μm fiber distances were not significantly different for any metrics assessed, the 700 μm distance did have significantly higher junction number, total length, and segment length compared to 300 μm and 900 μm groups. In RSC-laden scaffolds, the 300 μm group showed the strongest tube formation effect, with significantly higher junction number (28.63 ± 5.60 junctions mm^{-2}), total length ($7.59 \pm 1.46 \times 10^3$ μm mm^{-2}), and segment length ($2.13 \pm 0.56 \times 10^3$ μm mm^{-2}) than other fiber distance groups. There was no difference observed between 500 μm and 700 μm. The 900 μm group showed the weakest tube formation response. A direct comparison between RSC-free and RSC-laden scaffolds highlighted that the 300 μm RSC-laden scaffold was the most effective in promoting vascular network formation across all groups (figures 5(b)–(d)).

For RSC-free scaffolds, the network formation responses within each group were distinct depending on the fiber distance. In the 300 μm group, HMVECs tended to align closely along the fibers, with limited ability to branch between them (6.04 ± 3.52 junctions mm^{-2}). Meanwhile, the 900 μm group exhibited cells growing as a monolayer across the wide gaps with similarly low levels of branching (6.88 ± 3.46 junctions mm^{-2}). At 500 μm and 700 μm groups, however, HMVECs were able to form branching networks between adjacent fibers (13.94 ± 9.68 junctions mm^{-2} and 18.63 ± 9.70 junctions mm^{-2}, respectively). Thus, the optimal response observed at 700 μm can be explained by geometric constraints. In contrast, for RSC-laden scaffolds, network formation improved with decreasing fiber distance, with the 300 μm group showing the strongest effect. This suggests that at narrower distances, HMVECs are more effectively influenced by paracrine signals from RSCs, consistent with our gene expression results, which showed upregulation of pro-angiogenic genes in fiber-seeded RSCs.

To further investigate vascular network formation in a more physiological environment, we embedded HMVECs into collagen hydrogels. Collagen, the main component of the extracellular matrix (ECM), provides a supportive environment for cell growth and tissue regeneration. In particular, type I collagen hydrogels are widely used in vascularized tissue engineering as they promote EC proliferation, migration, and sprouting [84, 85]. CD31, a well-defined endothelial marker expressed on the surface of EC and used for monitoring vessel density [86], was chosen to assess 3D vascular networks in this study.

As shown in figure S4, we tested two collagen concentrations (1.5 mg ml^{-1} and 3 mg ml^{-1}), each containing 2×10^6 cells ml^{-1} of HMVECs, and seeded on the geltrex surface for 3 d. CD31 staining revealed that HMVECs formed firmer and more branched structures within the 1.5 mg ml^{-1} collagen compared to

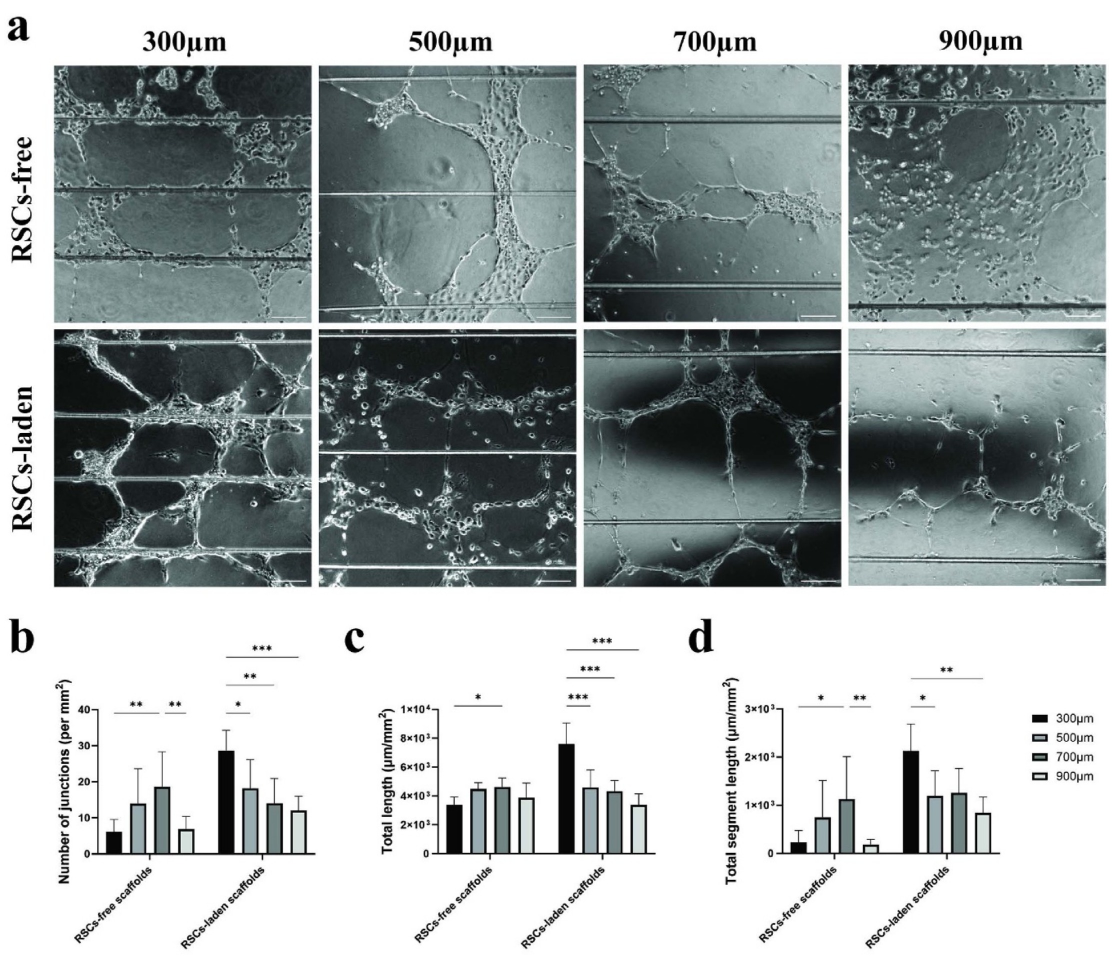

Figure 5. 2D tube formation of HMVECs with RSC-free and RSC-laden scaffolds after 16 h. (a) Brightfield images of HMVECs morphology within the parallel fibers among each group. Quantitative analysis was performed among each group to evaluate (b) number of junctions, (c) total length, and (d) total segment length. These three parameters were normalized by mm^2. Scale bars are 150 μm (a). $^*p < 0.05$, $^{**}p < 0.01$, $^{***}p < 0.001$, two-way ANOVA with Tukey's multiple comparisons post-hoc test, $n \geqslant 4$.

the 3 mg ml^{-1} group. We suggest the stiffer 3 mg ml^{-1} hydrogel limited HMVECs migration, while the softer 1.5 mg ml^{-1} hydrogel provided a more conducive environment. This is consistent with previous findings that collagen concentrations between 1.2–1.9 mg ml^{-1} could promote stable sprout formation as they allow endothelial proliferation and migration [87].

We next optimized the culture period for the 3D tube formation test by observing 1.5 mg ml^{-1} collagen hydrogels at different time points (figure S5). After 16 h, HMVECs did not form clear vascular network structures. At day 3, HMVECs developed clear branching structures inside the gel. With extended culture (days 5 and 7), the structures began to regress, showing reduced stability over time. Compared to the 2D test, in which vascular networks formed within 16 h and degraded by day 3 (figure S5), HMVECs took a longer time to sprout and branch, but experienced structural fading after 3 d. Based on these results, day 3 was selected as the optimal time point for the 3D tube formation test.

This difference between 2D and 3D tests can be explained by the different environments. When HMVECs are in contact with the 2D geltrex surface directly, they can migrate rapidly, resulting in a fast but short-term network formation. Cell migration in 3D collagen is slower, therefore, it takes longer to create the vascular networks. Previous studies have shown that co-culture with fibroblasts or adipose-derived stromal cells enables vascular networks to develop by day 3 and survive for over 14 d under optimized medium conditions [85, 88]. Our 3D vascular structures started to fade away after 3 d, likely due to the absence of supportive stromal cells.

After 3 d of culture, samples were fixed and stained with CD31 to assess network formation in the presence or absence of RSCs-laden scaffolds (figure 6). In the RSCs-free scaffolds, no significant differences were observed among the fiber distance groups, all showed comparable vessel area, junction number, and total length. In contrast, for the RSCs-laden scaffolds, the 300 μm group exhibited significantly higher network formation effects

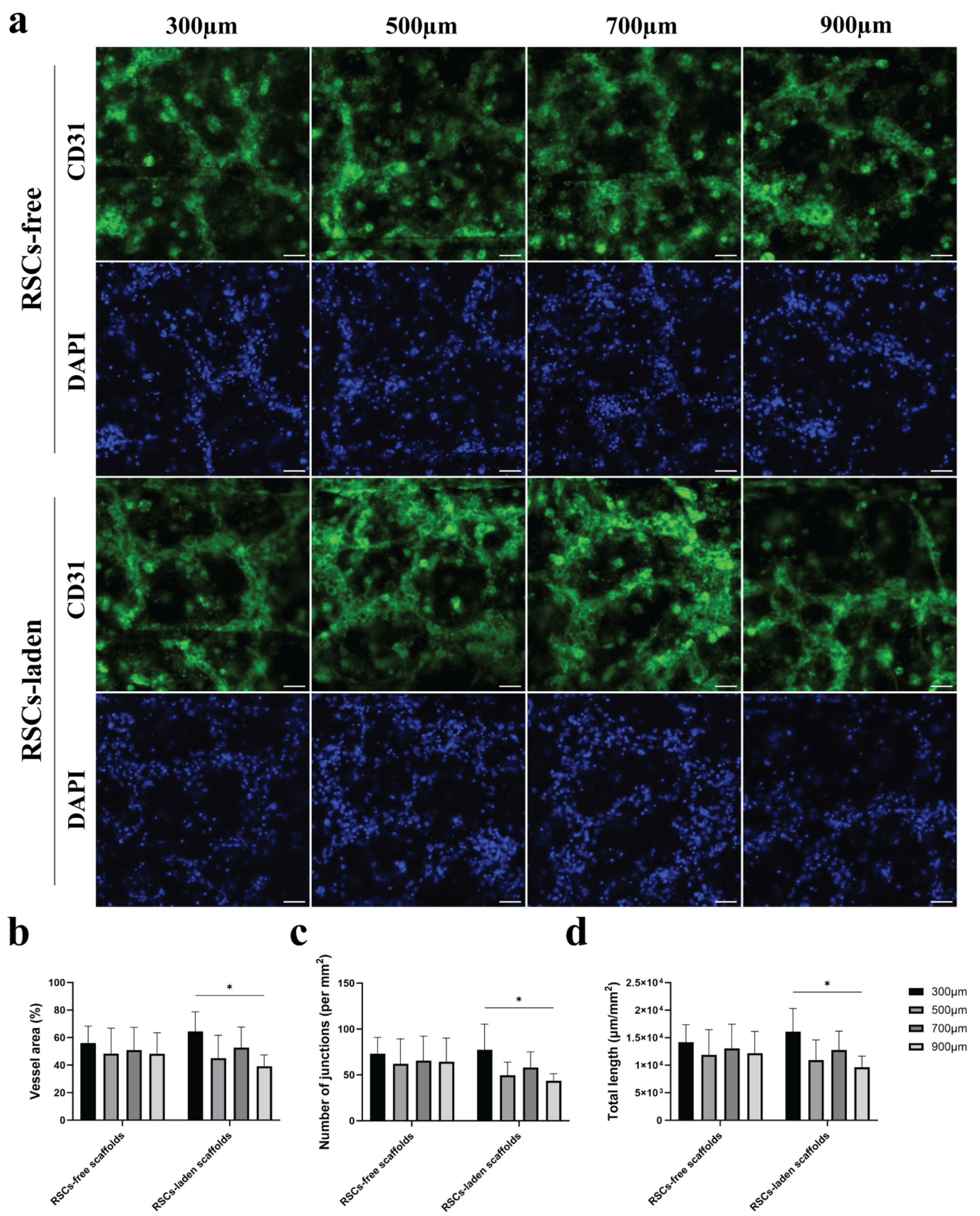

Figure 6. 3D tube formation of HMVECs with RSC-free and RSC-laden scaffolds after 3 d. (a) CD31 and DAPI staining of HMVECs within 1.5 mg ml^{-1} collagen hydrogel among each group. Quantitative analysis was performed among each group to evaluate (b) vessel area, (c) number of junctions, and (d) total length. These three parameters were normalized by mm^2. Scale bars are 50 μm (a). $^*p < 0.05$, two-way ANOVA with Tukey's multiple comparisons post-hoc test, $n = 6$.

than the 900 μm group (vessel area: 64.52 ± 14.26% vs. 39.31 ± 8.03%; junction density: 77.46 ± 27.87 junctions mm^{-2} vs. 43.59 ± 7.70 junctions mm^{-2}; total length: $1.60 \pm 0.42 \times 10^4$ μm mm^{-2} vs. $0.96 \pm 0.20 \times 10^4$ μm mm^{-2}). Although no significant differences were detected among the 300, 500, and 700 μm groups, the 300 μm group still showed the highest values. In addition, the 300 μm RSCs-laden scaffolds also surpassed all RSCs-free groups, confirming the pro-angiogenic effect of RSCs.

When comparing the 3D tube formation results (figure 6) to the 2D results, again, we observed that 300 μm RSCs-laden scaffolds provided the strongest pro-angiogenic effect. However, the differences between fiber distances in 3D were less apparent than in 2D. This reflects the natural differences between 2D and 3D environments, with 3D culture offering a more biomimetic but also more restrictive environment. Furthermore, the use of rat-derived SCs may have limited cross-species paracrine

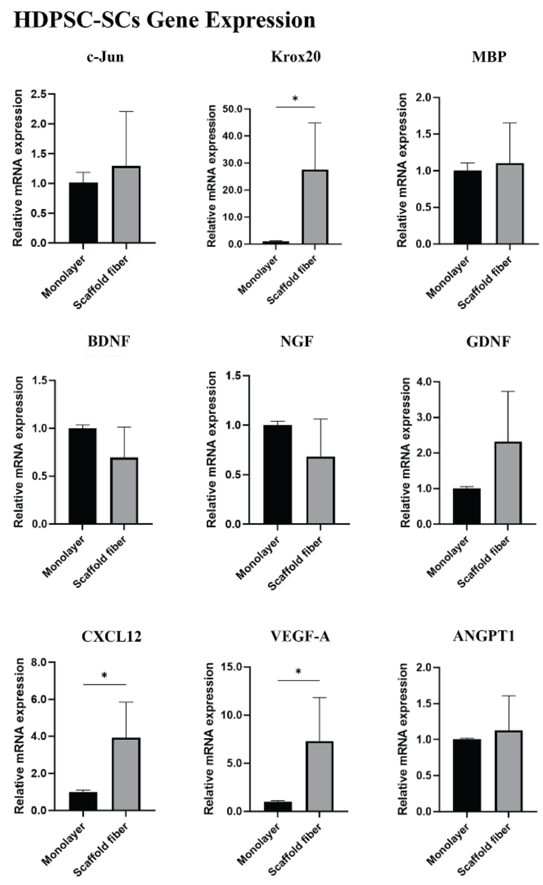

Figure 7. Gene expression of HDPSC-SCs on the MEW scaffolds compared to the monolayer culture after 1 d. $*p < 0.05$, unpaired t-test, $n = 3$.

signaling efficiency with human ECs, which helps to explain the smaller differences between RSCs-laden and RSCs-free groups in 3D than in 2D.

Overall, the 3D tube formation test confirmed the findings of the 2D test, that RSCs-laden scaffolds promote vascular network formation and a narrower fiber distance enhances this effect.

3.4. Effect of HDPSC-derived SCs on HMVEC network formation

To confirm the angiogenic capacity of human SCs, HDPSC-SCs were evaluated in comparison with RSCs. According to the results of 2D and 3D obtained with RSCs, the best performing group (300 μm MEW scaffolds) was selected for testing the effect of HDPSC-SCs.

We first assessed the gene expression profile of HDPSC-SCs after they were seeded on the MEW scaffolds (figure 7). Similar to RSCs, HDPSC-SCs showed significant upregulation of Krox20 (27.52-fold), CXCL12 (3.93-fold), and VEGF-A (7.32-fold). For other genes, including c-Jun, MBP, NGF, GDNF, and ANGPT1, no significant differences were shown between scaffold fiber and monolayer culture. The overall tendency in HDPSC-SCs was consistent with RSC results, showing upregulation of most genes except NGF. Interestingly, BDNF was also downregulated in HDPSC-SCs.

In contrast to RSCs, c-Jun and MBP were not highly upregulated in HDPSC-SCs, while Krox20 expression was significantly enhanced. This suggests that HDPSC-SCs were activated by the fiber environment and shifted towards an early myelinating-like phenotype but did not reach full maturation, as indicated by the limited MBP expression. Regarding neurotrophic factor genes, no significant differences were detected in scaffold fiber condition compared to monolayer culture, but the overall trend was similar to RSCs, with NGF downregulated and GDNF upregulated. The downregulation of BDNF showed a different response of HDPSC-SCs when facing the scaffold microenvironment. Notably, both CXCL12 and VEGF-A were significantly upregulated, suggesting that HDPSC-SCs, like RSCs, have the capacity to promote vascular network formation through paracrine signaling.

This was confirmed in our 2D coculture system (figure 8(a)) by the tube formation results of HMVECs when co-cultured with HDPSC-SCs. Compared to RSCs, HDPSC-SCs induced a significantly higher number of junctions (46.89 ± 8.89 junctions mm^{-2}), total length (9.07 ± 1.04 × 10^3 μm mm^{-2}), and total segment length (3.26 ± 0.93 × 10^3 μm mm^{-2}) (figures 8(b)–(d)). Figure 8(a) also exhibits the 3D tube formation results. Here, HDPSC-SCs promoted a significantly higher total length compared to RSCs (2.07 ± 0.17 × 10^4 μm mm^{-2} vs. 1.61 ± 0.42 × 10^4 μm mm^{-2}), while vessel area and number of junctions showed no significant difference (figures 8(e)–(g)).

Overall, the 2D results clearly demonstrated a stronger pro-angiogenic effect of HDPSC-SCs than RSCs. In 3D, the enhancement was more limited, with only the total length being significantly higher. Taken together, these results indicate that HDPSC-SCs have a stronger angiogenic ability than RSCs in both 2D and 3D environments, consistent with our expectation that human-derived SCs interact with HMVECs. This effect was particularly shown in a 2D environment, whereas in 3D, the enhancement was less observed than expected.

Here, with the use of the MEW technique, we successfully fabricated scaffolds from medical-grade PCL, a widely used polymer in MEW due to its biocompatibility and mechanical properties [89, 90]. These scaffolds were designed with variable fiber distances to support SCs seeding at defined spacing intervals. This allowed us to demonstrate that SCs play a supportive role in promoting HMVEC organization within the 2D and 3D environments. Reduced fiber distance enhanced angiogenic effects, indicating that higher SC density may create a stronger pro-angiogenic niche. This highlights the importance of scaffold architecture in regulating

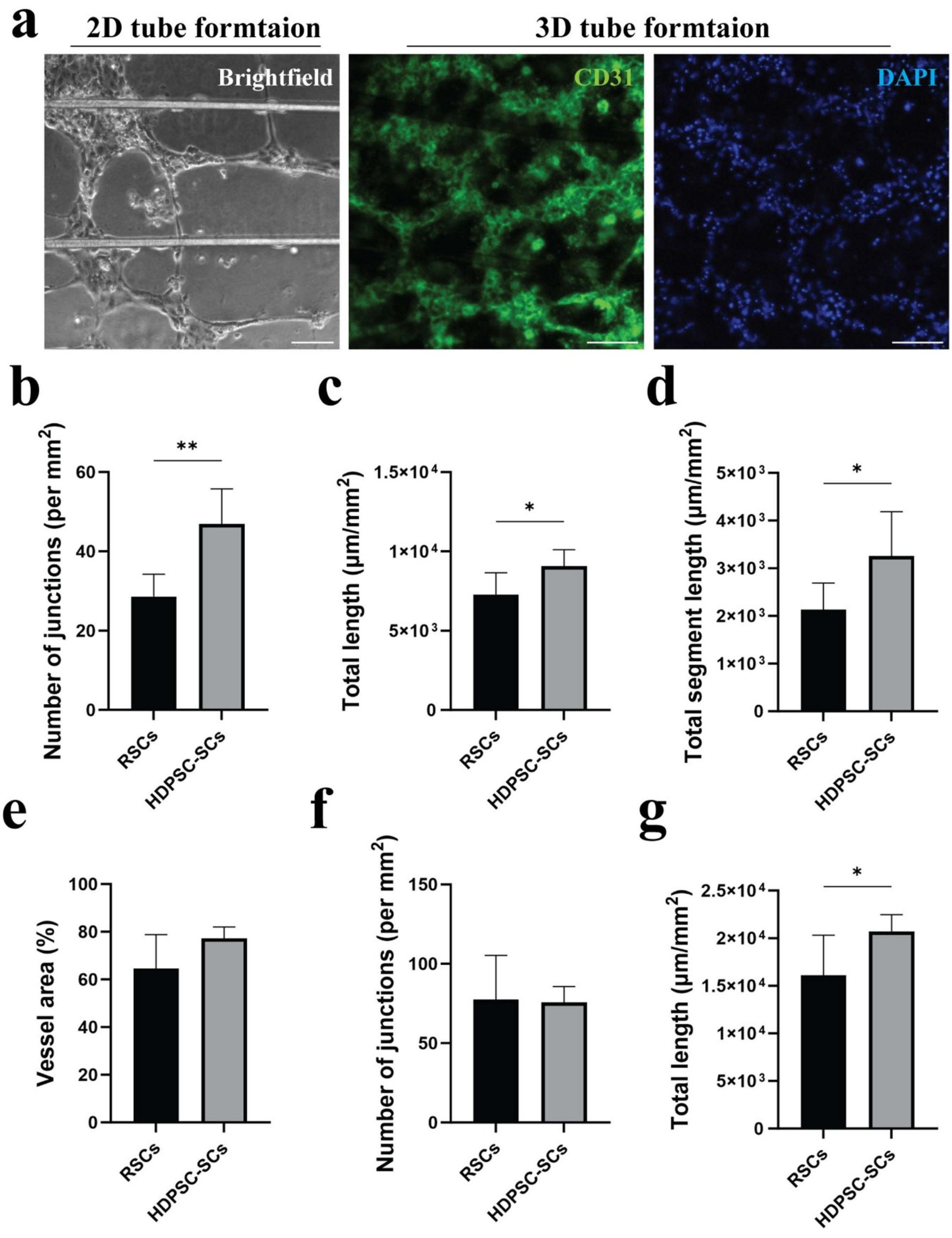

Figure 8. 2D and 3D tube formation of HMVECs with HDPSC-SCs-laden scaffolds. (a) Brightfield of HMVECs morphology after cultured with HDPSC-SCs for 16 h, and CD31/DAPI staining of HMVECs after cultured with HDPSC-SCs for 3 d. Quantitative analysis was performed to evaluate (b) number of junctions, (c) total length, (d) total segment length, (e) vessel area, (f) number of junctions, and (g) total length. The parameters were normalized by mm^2. Scale bars are 100 μm (a), (e). $^*p < 0.05$, $^{**}p < 0.01$, unpaired t-test, $n \geqslant 5$.

intercellular interactions and further emphasizes the pro-angiogenic role of SCs beyond their classical function in nerve myelination and regeneration.

To investigate SC–HMVEC interactions on suspended single fibers, we combined MEW scaffolds with customized PDMS seeding and co-culture systems. By integrating region-specific scaffold design, PDMS support structures, and optimized seeding procedures, we established a controllable and repeatable platform to study neurovascular interactions in both 2D and 3D environments. Importantly, the MEW fibers in this system were not intended to mimic neuron axons but to serve as topographical tools that reproduce variations in SC alignment spacing under well-defined settings. Notably, the differences in angiogenic effects observed between

HDPSC-SCs and RSCs underscore the value of using human-derived cell sources for translational tissue engineering studies. Furthermore, by systematically adjusting fiber distance within a region-specific scaffold architecture, we demonstrate that parallel single fiber topography cues can serve as a controllable biological signal to modulate SCs phenotype and angiogenic signaling, extending the role of MEW from a structural fabrication tool to a biologically instructive platform for neurovascular engineering.

While this study demonstrates the effect of SCs on vascular network formation, it focuses on structural features of vascular network development rather than functional properties such as perfusion, maturation, or host integration. *In vivo* models provide a powerful approach to evaluate these functional aspects, as they enable assessment of vascular stability, anastomosis with host vessels, and long-term neurovascular coupling. Although the current MEW scaffold design allows for high-resolution analysis of neurovascular interactions in a well-controlled *in vitro* environment, the relatively small and highly defined functional region raises practical challenges for direct implantation and functional vascular assessment *in vivo*. Future studies should therefore focus on scaling and adjusting the scaffold architecture, such as expanding the functional area and optimizing the fiber distance and SCs density, to enable *in vivo* evaluation of vascular function and neurovascular integration.

4. Conclusion

In this study, we fabricated MEW scaffolds with parallel fibers to mimic the peripheral nerve microenvironment for SCs seeding. The scaffolds showed good SC adhesion, viability, and gene expression analysis revealed not only neurotrophic and myelination-related gene upregulation but also significantly enhanced upregulation of pro-angiogenic genes. When co-cultured with HMVECs in both 2D and 3D environments, SCs-laden scaffolds strongly promoted vascular network formation. By varying fiber distance and comparing RSCs to HDPSC-SCs, we found that the smaller fiber distance, the stronger angiogenic responses, with human-derived SCs exhibiting superior pro-angiogenic potential. Collectively, these findings demonstrate MEW scaffolds as a flexible tool for studying neurovascular interactions. The versatility of this coculture system presents the possibility of creating more mimetic conditions found in the body, such as exploring ECM composition and matrix signaling, the inclusion of neurons or other cells within the 3D matrix, and the use of patient-derived cells to model specific cell–cell and cell-matrix interactions in the context of diseases (e.g. neural injury, neuropathies, Charcot–Marie–Tooth disease). These new insights into SC-mediated modulation of vascular network formation also underscore the potential of using scaffold to incorporate SCs for controlled neurovascularization of *in vitro* models as well as engineered tissues.

Acknowledgment

This work was supported by the European Research Council (ERC) under the ERC StG Project OviChip (Grant No. 101043014); the China Scholarship Council (Grant No. 202206170025); and LINK2.0, a project funded by Maastricht University and the Academic Hospital Maastricht.

Data availability statement

All data that support the findings of this study are included within the article (and any supplementary files).

Supplementary Figures & Tables available at https://doi.org/10.1088/1758-5090/ae4ccc/data1.

ORCID iDs

Hao Wu 0000-0002-3240-0522
Nathalie Dirkx 0000-0002-1942-3172
Esther Wolfs 0000-0001-9277-6524
Lorenzo Moroni 0000-0003-1298-6025
Paul Wieringa 0000-0002-3290-5125

References

[1] Guo X, Elliott C G, Li Z, Xu Y, Hamilton D W and Guan J 2012 Creating 3D angiogenic growth factor gradients in fibrous constructs to guide fast angiogenesis *Biomacromolecules* **13** 3262–71

[2] Nillesen S T M, Geutjes P J, Wismans R, Schalkwijk J, Daamen W F and van Kuppevelt T H 2007 Increased angiogenesis and blood vessel maturation in acellular collagen–heparin scaffolds containing both FGF2 and VEGF *Biomaterials* **28** 1123–31

[3] Mercado-Pagán Á E, Stahl A M, Shanjani Y and Yang Y 2015 Vascularization in bone tissue engineering constructs *Annu. Biomed. Eng.* **43** 718

[4] Muangsanit P, Shipley R J and Phillips J B 2018 Vascularization strategies for peripheral nerve tissue engineering *Anat. Rec.* **301** 1657

[5] Yapici A K, Bayram Y, Akgun H, Gumus R and Zor F 2017 The effect of *in vivo* created vascularized neurotube on peripheric nerve regeneration *Injury* **48** 1486–91

[6] Thibodeau A, Galbraith T, Fauvel C M, Khuong H T and Berthod F 2022 Repair of peripheral nerve injuries using a prevascularized cell-based tissue-engineered nerve conduit *Biomaterials* **280** 121269

[7] Phua Q H, Han H A and Soh B-S 2021 Translational stem cell therapy: vascularized skin grafts in skin repair and regeneration *J. Transl. Med.* **19** 1–11

[8] Miyazaki H, Tsunoi Y, Akagi T, Sato S, Akashi M and Saitoh D 2019 A novel strategy to engineer pre-vascularized 3-dimensional skin substitutes to achieve efficient, functional engraftment *Sci. Rep.* **9** 1–10

[9] Beyer S, Koch M, Lee Y H, Jung F and Blocki A 2018 An *in vitro* model of angiogenesis during wound healing provides insights into the complex role of cells and factors in the inflammatory and proliferation phase *Int. J. Mol. Sci.* **19** 2913

[10] Hofmann E, Fink J, Pignet A-L, Schwarz A, Schellnegger M, Nischwitz S P, Holzer-Geissler J C J, Kamolz L-P and Kotzbeck P 2023 Human *in vitro* skin models for wound

healing and wound healing disorders *Biomedicines* **11** 1056

[11] Ramasamy S K *et al* 2016 Blood flow controls bone vascular function and osteogenesis *Nat. Commun.* **7** 1–13

[12] Morgan E F, Hussein A I, Al-Awadhi B A, Hogan D E, Matsubara H, Al-Alq Z, Fitch J, Andre B, Hosur K and Gerstenfeld L C 2012 Vascular development during distraction osteogenesis proceeds by sequential intramuscular arteriogenesis followed by intraosteal angiogenesis *Bone* **51** 535

[13] Sriram G, Handral H K, Uin Gan S, Islam I, Jalil Rufaihah A and Cao T 2020 Fabrication of vascularized tissue constructs under chemically defined culture conditions *Biofabrication* **12** 045015

[14] Kim J J, Hou L and Huang N F 2016 Vascularization of three-dimensional engineered tissues for regenerative medicine applications *Acta Biomater.* **41** 17–26

[15] Hou T, Du M, Gao X and An M 2022 Human vascular endothelial cells promote the secretion of vascularization factors and migration of human skin fibroblasts under co-culture and its preliminary application *Int. J. Mol. Sci.* **23** 13995

[16] Vidal S E L, Tamamoto K A, Nguyen H, Abbott R D, Cairns D M and Kaplan D L 2019 3D biomaterial matrix to support long term, full thickness, immuno-competent human skin equivalents with nervous system components *Biomaterials* **198** 194–203

[17] Hsu Y-J, Wei S-Y, Lin T-Y, Fang L, Hsieh Y-T and Chen Y-C 2022 A strategy to engineer vascularized tissue constructs by optimizing and maintaining the geometry *Acta Biomater.* **138** 254–72

[18] Bahr-Hosseini M and Bikson M 2021 Neurovascular-modulation: a review of primary vascular responses to transcranial electrical stimulation as a mechanism of action *Brain Stimul.* **14** 837–47

[19] Malheiro A, Wieringa P and Moroni L 2021 Peripheral neurovascular link: an overview of interactions and *in vitro* models *Trends Endocrinol. Metab.* **32** 623–38

[20] Elorza Ridaura I, Sorrentino S and Moroni L 2021 Parallels between the developing vascular and neural systems: signaling pathways and future perspectives for regenerative medicine *Adv. Sci.* **8** e2101837

[21] Adams R H and Alitalo K 2007 Molecular regulation of angiogenesis and lymphangiogenesis *Nat. Rev. Mol. Cell Biol.* **8** 464–78

[22] Demir R, Seval Y and Huppertz B 2007 Vasculogenesis and angiogenesis in the early human placenta *Acta Histochem.* **109** 257–65

[23] Li W, Kohara H, Uchida Y, James J, Soneji K, Cronshaw D, Zou Y-R, Nagasawa T and Mukouyama Y-S 2013 Peripheral nerve-derived CXCL12 and VEGF-A regulate the patterning of arterial vessel branching in developing limb skin *Dev. Cell* **24** 359–71

[24] Mukouyama Y-S, Gerber H-P, Ferrara N, Gu C and Anderson D J 2005 Peripheral nerve-derived VEGF promotes arterial differentiation via neuropilin 1-mediated positive feedback *Development* **132** 941–52

[25] Gao D, Sun H, Zhu J, Tang Y and Li S 2018 CXCL12 induces migration of Schwann cells via p38 MAPK and autocrine of CXCL12 by the CXCR4 receptor *Int. J. Clin. Exp. Pathol.* **11** 3119

[26] Taiana M M, Lombardi R, Porretta-Serapiglia C, Ciusani E, Oggioni N, Sassone J, Bianchi R and Lauria G 2014 Neutralization of Schwann cell-secreted VEGF is protective to *in vitro* and *in vivo* experimental diabetic neuropathy *PLoS One* **9** e108403

[27] Wang L, Chopp M, Szalad A, Lu X, Lu M, Zhang T and Zhang Z G 2018 Angiopoietin-1/Tie2 signaling pathway contributes to the therapeutic effect of thymosin β4 on diabetic peripheral neuropathy *Neurosci. Res.* **147** 1

[28] Huang J-H, Chen Y-N, He H, Fu C-H, Xu Z-Y and Lin F-Y 2023 Schwann cells-derived exosomes promote functional recovery after spinal cord injury by promoting angiogenesis *Front. Cell Neurosci.* **16** 1077071

[29] Rayner M E L I S S A L D, Laranjeira S, Evans R E, Shipley R J, Healy J and Phillips J B 2018 Developing an *in vitro* model to screen drugs for nerve regeneration *Anat. Rec.* **301** 1628

[30] Park S E, Ahn J, Jeong H-E, Youn I, Huh D and Chung S 2021 A three-dimensional *in vitro* model of the peripheral nervous system *NPG Asia Mater.* **13** 1–11

[31] Andersen N D and Monje P V 2018 Isolation, culture, and cryopreservation of adult rodent Schwann cells derived from immediately dissociated teased fibers *Methods Mol. Biol.* **1739** 49–66

[32] Stratton J A, Kumar R, Sinha S, Shah P, Stykel M, Shapira Y, Midha R and Biernaskie J 2017 Purification and characterization of Schwann cells from adult human skin and nerve *eNeuro* **4** ENEURO.0307–16.2017

[33] Libberecht K, Dirkx N, Vangansewinkel T, Vandendries W, Lambrichts I and Wolfs E 2024 The influence of lysosomal stress on dental pulp stem cell-derived Schwann cells *Biomolecules* **14** 405

[34] Martens W, Sanen K, Georgiou M, Struys T, Bronckaers A, Ameloot M, Phillips J and Lambrichts I 2014 Human dental pulp stem cells can differentiate into Schwann cells and promote and guide neurite outgrowth in an aligned tissue-engineered collagen construct *in vitro* *FASEB J.* **28** 1634

[35] Yang K, Yang S, Teng X, He X, Sun T and Chen H 2025 Modulating Schwann cell behavior via functional nerve guidance conduits for enhanced peripheral nerve regeneration *npj Regen. Med.* **10** 54

[36] Panzer K V, Burrell J C, Helm K V T, Purvis E M, Zhang Q, Le A D, O'Donnell J C and Cullen D K 2020 Tissue engineered bands of Büngner for accelerated motor and sensory axonal outgrowth *Front. Bioeng. Biotechnol.* **8** 580654

[37] Lotfi L, Khakbiz M, Moosazadeh Moghaddam M and Bonakdar S 2019 A biomaterials approach to Schwann cell development in neural tissue engineering *J. Biomed. Mater. Res. A* **107** 2425–46

[38] Smith C S, Orkwis J A, Bryan A E, Xu Z and Harris G M 2022 The impact of physical, biochemical, and electrical signaling on Schwann cell plasticity *Eur. J. Cell Biol.* **101** 151277

[39] Subramanian A, Krishnan U M and Sethuraman S 2009 Development of biomaterial scaffold for nerve tissue engineering: biomaterial mediated neural regeneration *J. Biomed. Sci.* **16** 108

[40] Zhang X, Xu Z, Qiao Z, Wang H, Peng L and Dai K 2024 Highly architectural MEW scaffolds with superior performance *Mater. Des.* **245** 113290

[41] Brown T D, Dalton P D and Hutmacher D W 2011 Direct writing by way of melt electrospinning *Adv. Mater.* **23** 5651–7

[42] Chew S Y, Mi R, Hoke A and Leong K W 2007 The effect of the alignment of electrospun fibrous scaffolds on Schwann cell maturation *Biomaterials* **29** 653

[43] Li Y, Lv S, Yuan H, Ye G, Mu W, Fu Y, Zhang X, Feng Z, He Y and Chen W 2021 Peripheral nerve regeneration with 3D printed bionic scaffolds loading neural crest stem cell derived Schwann cell progenitors *Adv. Funct. Mater.* **31** 2010215

[44] Youssef A, Hrynevich A, Fladeland L, Balles A, Groll J, Dalton P D and Zabler S 2019 The impact of melt electrowritten scaffold design on porosity determined by x-ray microtomography *Tissue Eng. C* **25** 367

[45] Hrynevich A, Achenbach P, Jungst T, Brook G A and Dalton P D 2021 Design of suspended melt electrowritten fiber arrays for Schwann cell migration and neurite outgrowth *Macromol. Biosci.* **21** 2000439

[46] Snow F, Doyle S E, Liu E, Rauch D D, Millett D, Wilding-Mcbride J, Kita M, Pirogova E, Kapsa R M I and Quigley A 2025 A detailed guide to melt electro-writing for tissue engineering applications *Biofabrication* **17** 042004

[47] Xie C, Gao Q, Wang P, Shao L, Yuan H, Fu J, Chen W and He Y 2019 Structure-induced cell growth by 3D printing

of heterogeneous scaffolds with ultrafine fibers *Mater. Des.* **181** 108092

[48] Nguyen N T *et al* 2019 Identification of sagging in melt-electrospinning of microfiber scaffolds *Mater. Sci. Eng. C* **103** 109785

[49] Jørgensen M L, Müller C, Sikkersoq M, Nadzieja M, Zhang Z, Su Y, Just J, Garm Spindler K-L and Chen M 2020 A melt-electrowritten filter for capture and culture of circulating colon cancer cells *Mater. Today Bio* **6** 100052

[50] Zhang Y, Zhang Z, Wang Y, Su Y and Chen M 2020 3D myotube guidance on hierarchically organized anisotropic and conductive fibers for skeletal muscle tissue engineering *Mater. Sci. Eng. C* **116** 111070

[51] Agarwal K, Sahay R and Baji A 2020 Tensile properties of composite reinforced with three-dimensional printed fibers *Polymers* **12** 1089

[52] Malheiro A, Morgan F, Baker M, Moroni L and Wieringa P 2020 A three-dimensional biomimetic peripheral nerve model for drug testing and disease modelling *Biomaterials* **257** 120230

[53] Malheiro A, Harichandan A, Bernardi J, Seijas-Gamardo A, Konings G F, Volders P G A, Romano A, Mota C, Wieringa P and Moroni L 2021 3D culture platform of human iPSCs-derived nociceptors for peripheral nerve modeling and tissue innervation *Biofabrication* **14** 014105

[54] Kaewkhaw R, Scutt A M and Haycock J W 2012 Integrated culture and purification of rat Schwann cells from freshly isolated adult tissue *Nat. Protoc.* **7** 1996–2004

[55] Carpentier G, Berndt S, Ferratge S, Rasband W, Cuendet M, Uzan G and Albanese P 2020 Angiogenesis analyzer for ImageJ—A comparative morphometric analysis of “endothelial tube formation assay” and “fibrin bead assay” *Sci. Rep.* **10** 1–13

[56] Zudaire E, Gambardella L, Kurcz C, Vermeren S and Ruhrberg C 2011 A computational tool for quantitative analysis of vascular networks *PLoS One* **6** e27385

[57] Yao T, Wieringa P A, Chen H, Amit C, Samal P, Giselbrecht S, Baker M B and Moroni L 2020 Fabrication of a self-assembled honeycomb nanofibrous scaffold to guide endothelial morphogenesis *Biofabrication* **12** 045001

[58] Yang L, Wang X, Xiong M, Liu X, Luo S, Luo J and Wang Y 2024 Electrospun silk fibroin/fibrin vascular scaffold with superior mechanical properties and biocompatibility for applications in tissue engineering *Sci. Rep.* **14** 3942

[59] Kim J, Bakirci E, O’Neill K L, Hrynevich A and Dalton P D 2021 Fiber bridging during melt electrowriting of poly(ε-Caprolactone) and the influence of fiber diameter and wall height *Macromol. Mater. Eng.* **306** 2000685

[60] Stanton-Hicks M 2018 Anatomy and physiology related to peripheral nerve stimulation *Neuromodulation: Comprehensive Textbook of Principles, Technologies, and Therapies, Second Edition* vol 2 (Academic) pp 723–7

[61] Akaishi T 2017 New theoretical model of nerve conduction in unmyelinated nerves *Front. Physiol.* **8** 798

[62] Wang H B, Mullins M E, Cregg J M, McCarthy C W and Gilbert R J 2010 Varying the diameter of aligned electrospun fibers alters neurite outgrowth and Schwann cell migration *Acta Biomater.* **6** 2970–8

[63] Gnavi S, Fornasari B E, Tonda-Turo C, Ciardelli G, Zanetti M, Geuna S and Perroteau I 2015 The influence of electrospun fibre size on Schwann cell behaviour and axonal outgrowth *Mater. Sci. Eng. C* **48** 620–31

[64] Puhl D L, Funnell J L, Nelson D W, Gottipati M K and Gilbert R J 2020 Electrospun fiber scaffolds for engineering glial cell behavior to promote neural regeneration *Bioengineering* **8** 4

[65] Salzer J L 2015 Schwann cell myelination *Cold Spring Harb. Perspect. Biol.* **7** a020529

[66] Sherman D L and Brophy P J 2005 Mechanisms of axon ensheathment and myelin growth *Nat. Rev. Neurosci.* **6** 683–90

[67] Cámara-Torres M, Sinha R, Mota C and Moroni L 2020 Improving cell distribution on 3D additive manufactured scaffolds through engineered seeding media density and viscosity *Acta Biomater.* **101** 183–95

[68] Cucu P, Melinte V, Petrovici A R, Anghel N, Apostol I, Mares M, Simionescu N and Spiridon I 2025 A biopolymeric dextran-chitosan delivery system for controlled release of antioxidant and anti-inflammatory compounds: lignin and curcumin *Molecules* **30** 1276

[69] Arthur-Farraj P J *et al* 2012 c-Jun reprograms Schwann cells of injured nerves to generate a repair cell essential for regeneration *Neuron* **75** 633–47

[70] Parkinson D B *et al* 2008 c-Jun is a negative regulator of myelination *J. Cell Biol.* **181** 625

[71] Jessen K R and Mirsky R 2019 The success and failure of the Schwann cell response to nerve injury *Front. Cell Neurosci.* **13** 33

[72] Schepers M, Malheiro A, Gamardo A S, Hellings N, Prickaerts J, Moroni L, Vanmierlo T and Wieringa P 2023 Phosphodiesterase (PDE) 4 inhibition boosts Schwann cell myelination in a 3D regeneration model *Eur. J. Pharm. Sci.* **185** 106441

[73] Liu Z, Jin Y-Q, Chen L, Wang Y, Yang X, Cheng J, Wu W, Qi Z and Shen Z 2015 Specific Marker expression and cell State of Schwann cells during culture *in vitro PLoS One* **10** e0123278

[74] Kim H-S, Lee J, Lee D Y, Kim Y-D, Kim J Y, Lim H J, Lim S and Cho Y S 2017 Schwann cell precursors from human pluripotent stem cells as a potential therapeutic target for myelin repair *Stem Cell Rep.* **8** 1714

[75] Yi S, Yuan Y, Chen Q, Wang X, Gong L, Liu J, Gu X and Li S 2016 Regulation of Schwann cell proliferation and migration by MIR-1 targeting brain-derived neurotrophic factor after peripheral nerve injury *Sci. Rep.* **6** 1–10

[76] Höke A, Ho T, Crawford T O, LeBel C, Hilt D and Griffin J W 2003 Glial cell line-derived neurotrophic factor alters axon Schwann cell units and promotes myelination in unmyelinated nerve fibers *J. Neurosci.* **23** 561

[77] Shakhbazau A, Kawasoe J, Hoyng S A, Kumar R, van Minnen J, Verhaagen J and Midha R 2012 Early regenerative effects of NGF-transduced Schwann cells in peripheral nerve repair *Mol. Cell Neurosci.* **50** 103–12

[78] Piirsoo M, Kaljas A, Tamm K and Timmusk T 2010 Expression of NGF and GDNF family members and their receptors during peripheral nerve development and differentiation of Schwann cells *in vitro Neurosci. Lett.* **469** 135–40

[79] Brudno Y, Ennett-Shepard A B, Chen R R, Aizenberg M and Mooney D J 2013 Enhancing microvascular formation and vessel maturation through temporal control over multiple pro-angiogenic and pro-maturation factors *Biomaterials* **34** 9201–9

[80] Lovecchio J, Pannella M, Giardino L, Calzà L and Giordano E 2020 A dynamic culture platform enhances the efficiency of the 3D HUVEC-based tube formation assay *Biotechnol. Bioeng.* **117** 789–97

[81] Doshi R B, Vakil D, Molley T G, Islam M S, Kilian K A, Cunningham C and Sidhu K S 2024 Mesenchymal stem cell-secretome laden photopolymerizable hydrogels for wound healing *J. Biomed. Mater. Res. A* **112** 1484–93

[82] Faulkner A, Purcell R, Hibbert A, Latham S, Thomson S, Hall W L, Wheeler-Jones C and Bishop-Bailey D 2014 A thin layer angiogenesis assay: a modified basement matrix assay for assessment of endothelial cell differentiation *BMC Cell Biol.* **15** 41

[83] Shin J, Ahn S H and Oh D-J 2024 Pseudomonas aeruginosa N-3-Oxododecanoyl homoserine lactone disrupts endothelial integrity by activating the angiopoietin-tie system *Cell Biochem. Biophys.* **82** 1555–66

[84] Zhang Y, Kumar P, Lv S, Xiong D, Zhao H, Cai Z and Zhao X 2021 Recent advances in 3D bioprinting of vascularized tissues *Mater. Des.* **199** 109398

[85] Andrée B, Ichanti H, Kalies S, Heisterkamp A, Strauß S, Vogt P-M, Haverich A and Hilfiker A 2019 Formation of three-dimensional tubular endothelial cell networks under

defined serum-free cell culture conditions in human collagen hydrogels *Sci. Rep.* **9** 1–11

[86] Schlüter A *et al* 2018 CD31 and VEGF are prognostic biomarkers in early-stage, but not in late-stage, laryngeal squamous cell carcinoma *BMC Cancer* **18** 1–8

[87] Shamloo A, Mohammadaliha N, Heilshorn S C and Bauer A L 2016 A comparative study of collagen matrix density effect on endothelial sprout formation using experimental and computational approaches *Annu. Biomed. Eng.* **44** 929–41

[88] Ichanti H, Sladic S, Kalies S, Haverich A, Andrée B and Hilfiker A 2020 Characterization of tissue engineered endothelial cell networks in composite collagen-agarose hydrogels *Gels* **6** 27

[89] Wu X, Zhao F, Wang H, Schirhagl R and Włodarczyk-Biegun M K 2025 Integrating melt electrowriting (MEW) PCL scaffolds with fibroblast-laden hydrogel toward vascularized skin tissue engineering *Mater. Today Bio* **31** 101593

[90] Shahverdi M, Seifi S, Akbari A, Mohammadi K, Shamloo A and Movahhedy M R 2022 Melt electrowriting of PLA, PCL, and composite PLA/PCL scaffolds for tissue engineering application *Sci. Rep.* **12** 1–16